photonics

MDPI

Article

A Direct Measurement of the C_2H_2 Concentration from the C_2H_2–Oil Mixed Solution Using the Photoacoustic Spectroscopy Method

Zikang Rong [1], Jian Ke [2], Haifei Lu [1], Xiaoyan Wen [1], Lijie Li [3], Zhiwen Ming [2], Shuo Deng [1,2,*] and Min Li [1,*]

[1] School of Physics and Mechanics, Wuhan University of Technology, Wuhan 430070, China; 333615@whut.edu.cn (Z.R.); haifeilv@whut.edu.cn (H.L.); wenxy@whut.edu.cn (X.W.)
[2] Wuhan Yusheng Optoelectronic Co., Ltd., Wuhan 430200, China; kejian@ysod.com (J.K.); mzw@ysod.com (Z.M.)
[3] Faculty of Science and Engineering, Swansea University, Swansea SA1 8EN, UK; l.li@swansea.ac.uk
* Correspondence: dengshuo1990@whut.edu.cn (S.D.); minli@whut.edu.cn (M.L.)

Abstract: The photoacoustic (PA) method is commonly used in the measurement of trace gas concentration owing to its high accuracy and reliability. However, the conventional PA method is usually used in the gas-phase environment, which leads to a long measurement time and a large equipment volume for the degassing process. In this paper, we report a scheme to measure the acetylene (C_2H_2) concentration from the acetylene–dielectric oil (C_2H_2–Oil) mixed solution without the degassing process. The frequency and intensity distribution of the PA signal in the C_2H_2–Oil mixed liquid is investigated using the finite element method (FEM). Simulation results reveal that the incident light modulation frequency and the geometry size of the PA cell are two core factors to determine the PA signal. Furthermore, a PA sensor system is constructed to measure the concentration of C_2H_2 from the C_2H_2–Oil mixed solution. The measurement results demonstrate that the intensity of the PA signal in the C_2H_2–Oil mixed solution rises mostly linearly with the concentration of C_2H_2 from 0 to 100 mL/L. The Allan variance results from the continuous tests indicate that the measurement limit of the PA sensor system is about 0.2 mL/L. This work points to a novel method for the measurement of the C_2H_2 concentration from the C_2H_2–Oil mixed solution.

Keywords: photoacoustic spectroscopy; gas–liquid mixed solution; direct measurement; acetylene concentration

Received: 18 March 2025
Revised: 29 April 2025
Accepted: 8 May 2025
Published: 10 May 2025

Citation: Rong, Z.; Ke, J.; Lu, H.; Wen, X.; Li, L.; Ming, Z.; Deng, S.; Li, M. A Direct Measurement of the C_2H_2 Concentration from the C_2H_2–Oil Mixed Solution Using the Photoacoustic Spectroscopy Method. *Photonics* **2025**, *12*, 471. https://doi.org/10.3390/photonics12050471

1. Introduction

In recent years, photoacoustic (PA) sensors have been widely used in oil-filled electrical equipment because they have some advantages such as high sensitivity and a rapid detection time without requiring calibration [1–5]. The PA sensor typically comprises three core components: a light source, a PA cell, and a microphone [6]. The technological progress of each of the above components usually contributes to the improvement of the PA sensor. Thanks to the development of narrow linewidth and high-output power semiconductor lasers, the measurement accuracy of the PA sensor has significantly improved [7]. In 2000, M. Wolff et al. [8] reported a PA sensor based on the distributed feedback (DFB) laser, which can be tuned directly. The direct frequency modulation of the DFB laser avoids the coherent noise from using chopper and then contributes to higher measurement precision. In 2005, J.P. Besson et al. [9] reported a PA sensor using a near-infrared tunable DFB laser.

This PA sensor could simultaneously measure the concentrations of methane (CH_4), water (H_2O), and hydrogen chloride (HCl) gasses. In addition, with the development of a precise fabrication technique, the sensitivity of the microphone is also improved. The sensitivity from −43.5 dB (capacitive microphones) increased to about −10.9 dB (Fabry–Perot cantilever microphone) in 12 years [10–12]. Furthermore, the optimized PA cell structure also contributes to the improvement of the measurement accuracy of the PA sensor. Y. Ma et al. [13] proposed a high-sensitivity PA sensor using a retro-reflection-cavity-enhanced PA cell structure, which effectively suppressed the gas flow noise and enhanced the intensity of the PA signal. Using this type of PA sensor, the measurement accuracy of acetylene (C_2H_2) gas achieved about 138 μL/L.

In prior works, the PA sensors are usually applied in the gas-phase environment. As a result, the degassing process was required. Therefore, conventional PA sensors have shown some disadvantages, such as a large volume of equipment and a long measurement time [14]. In fact, the PA effect also exists in the liquid and gas–liquid mixed-phase environments. In 1982, T. Kitamori et al. [15] studied the frequency characteristics of PA signals in the dye solution. They revealed that the resonance peak of the PA signal appeared at the incident light modulation frequency of about 100 kHz. In 2007, Y. Nosaka et al. [16] demonstrated that the PA effect also existed in sodium or benzene solutions. Currently, just a small number of works reported the direct measurement of dissolved gases using the PA method. J. Dai et al. [17] constructed a PA sensor to measure the concentration of carbon dioxide (CO_2) in water. They demonstrated that the intensity of the PA signal was proportional to the concentration of CO_2. Another work for the direct measurement of dissolved C_2H_2 from dielectric oil used the photothermal spectroscopy technology [18]. In their work, an oil–core photonic crystal fiber was used instead of the PA cell. The sensitivity of the sensor was about 1.4 μL/L.

Although the PA effect has been demonstrated in the gas–liquid mixed solution [17], to the best our knowledge, the characteristics of the PA signal in the C_2H_2–Oil mixed solution is still unclear. The concentration measurement of C_2H_2 from dielectric oil is very important for transformer fault monitoring [19]. Hence, in this work, we first study the frequency and intensity characteristics of the PA signal in the C_2H_2–Oil mixed solution. Our theoretical results reveal that the light modulation frequency and the geometry size of the PA cell are two core factors to dominate the PA signal. Then, we construct a PA sensor system to measure the different concentrations of C_2H_2 from the C_2H_2–Oil mixed solutions. This work provides a guideline for the direct measurement of C_2H_2 concentration using the PA method.

2. Theoretical Analysis of the PA Signal

In order to study the intensity and frequency characteristics of the PA signal in the C_2H_2–Oil mixed solution, the finite element method (FEM) is used. In prior studies, the FEM model is a classical method to investigate the frequency and intensity characteristics of the PA signal in the PA cell [20,21]. In the simulation, the C_2H_2–Oil mixed-phase environment is treated as an inviscid fluid, and the acoustic transducer is treated as a sound absorber [15]. If we assume that the dielectric oil is a viscid fluid medium, the degradation of the PA signal in the PA cell should be consider because a part of the sound wave is loss to heat due to viscous resistance [22]. As a result, the viscid fluid assumption could sharply increase the complexity of the FEM simulation. In fact, the error of the inviscid assumption mainly appears at the high C_2H_2 concentration range because the value of viscosity increases with increasing C_2H_2 concentration. In the low C_2H_2 concentration range, the inviscid assumption is reliable. Moreover, we assume that the distribution of the C_2H_2–Oil solution is axially symmetrical and that the thermal diffusion length is negligibly

shorter than the radius of the incident light beam. The axially symmetric distribution is a method to reduce the simulation time because the model of the PA cell could converse from three-dimensional (3D) to 2D.

The time and spatial distributions of the incident light beam are treated as a δ-function series and a Gaussian distribution, respectively. As long as the incident light is modulated, its wave function $I(r,t)$ can be expressed as follows [15]:

$$I(r,t) = I_m e^{-\frac{2s^2r^2}{r_0^2}} \sum_{n=0}^{[tf]} \delta(t - \frac{n}{f}) \tag{1}$$

where

$$s = \left(1 - \frac{\alpha I_m l}{\lambda \kappa} \frac{dn}{dT}\right)^{-1/2} \tag{2}$$

where r is the distance from the center of the C_2H_2–Oil mixed solution, f is the light modulation frequency, r_0 is the radius of the incident light beam, I_m is the maximum of the incident light power, λ is the center wavelength of the incident light, and l is the length of the PA cell. s, α, κ, n, and T are the light scattering coefficient, absorption coefficient, thermal conductivity, refractive index, and temperature of the C_2H_2–Oil mixed solution, respectively. $[x]$ is a Gaussian notation for the largest integer less than the number x in parentheses. The photon number of the incident light signal is inversely proportional to f. Hence, the relationship between $I(r,t)$ and the generated heat $H(r,t)$ can be written as follows:

$$H(r,t) = \frac{\alpha}{f} I(r,t) \tag{3}$$

From Equations (1) and (2), the wave function of the thermoelastic wave $p(r,t)$ in the C_2H_2–Oil mixed solution can be expressed as follows [23]:

$$\frac{1}{v^2}\frac{\partial^2}{\partial t^2} p(r,t) - \nabla^2 p(r,t) = \frac{\beta}{C_p} H(r,t) \tag{4}$$

where v, β, and C_p are the sound velocity, thermal expansion coefficient, and isobaric heat capacity in the C_2H_2–Oil solution, respectively.

In order to magnify the intensity of the PA signal, a typical dumbbell-shaped PA cell is usually used. Buffer cavities at both ends of the PA cell form an open chamber condition for noise reduction [24]. The narrower segment between the two buffer chambers is the resonant cavity. The symmetric external shape of the resonant cavity matches well with the axially symmetric light beam and the acoustic field [25]. From prior studies [26], the intensity of $p(r,t)$ at $r = a$ in the gas–liquid mixed solution can be expressed as follows:

$$P = [p(a,t) \cdot p^*(a,t)]^{\frac{1}{2}} = \sum_{m=0}^{l} \xi \frac{I_m}{f} R(a, r_0) A_m(a, r_0; f) \tag{5}$$

where

$$\xi = \frac{\pi^2}{\sqrt{2}} sv \frac{\alpha\beta}{C_p} \tag{6}$$

$$A_m(r, r_0; f) = e^{-\frac{4s^2v^2m^2}{r_0^2 f^2}} I_0\left(\frac{8s^2 rvm}{r_0^2 f}\right) \tag{7}$$

$$l = \left[\frac{r_0 f}{2sv}\right] \tag{8}$$

$$R(a, r_0) = \frac{1}{r_0} e^{-\frac{2s^2r^2}{r_0^2}} \left\{ {I_0}^2\left(\frac{2s^2r^2}{r_0^2}\right) + \frac{1}{\pi^2}{K_0}^2\left(\frac{2s^2r^2}{r_0^2}\right) \right\}^{\frac{1}{2}} \quad (9)$$

In Equations (4)–(8), I_0 and K_0 are the modified 0th-order Bessel function and the Hankel function, respectively.

The core parameters in the FEM simulation are shown in Table 1. From prior studies, when the length of the resonant cavity (L_r) and the buffer cavity (L_b) are 1/2 and 1/4 of the acoustic wave wavelength (λ) respectively, they are the optimal dimensions for suppressing noise. [27]. Therefore, L_b, L_r, and λ satisfy $L_b = 1/2L_r = 1/4\lambda$ in the FEM simulation. The C_2H_2–Oil mixed solution medium is consisted with 100 mL/L C_2H_2 and dielectric oil. The environment temperature is 300 K, and the incident light power is 10 mW.

Table 1. Core parameters for the FEM simulation.

Parameters	Value
a; cell radius	3.00 mm
C_p; isobaric heat capacity	1902 J/(kg·K) [28]
v; sound velocity	1420 m/s [29]
s; light scattering coefficient	0.08 1/cm
β; thermal expansion coefficient	0.0008 1/K [28]
α; C_2H_2 absorption coefficient	5.55×10^{-1} 1/cm [30]

Figure 1a,b show the sound pressure variation at the different lengths and radii of the resonant cavity, respectively. The preliminary sizes of the length and diameter of the resonant cavity are about 100 mm and 6 mm, respectively. Upon observing the frequency response curve of the sound pressure signal, a peak is observed. This is because a standing wave is formed within the resonant cavity, resulting in the enhancement of the sound pressure. Figure 1a shows that increasing the length of the resonant cavity from 50 to 150 mm slightly affects the peak intensity and the resonance frequency of the PA signal. This is because the incident light is quickly absorbed by the C_2H_2–Oil mixed solution. The sound pressure dependence of the resonant cavity radius is investigated using a fixed resonant cavity length of 75 mm. Clearly, the intensity of the sound pressure peak decreases as the radius of the resonant cavity increases, as shown in Figure 1b. Therefore, a smaller resonator radius is preferred. However, the radius of the resonator smaller than 3 mm may give rise to high PA background signals due to the absorption of the wings of the Gaussian light beam profile. Hence, the optimized resonant cavity geometry size can be achieved at the length of 75 mm and the radius of 3 mm. Based on this resonant cavity size, the influences of the buffer cavity length and radius on the sound pressure are investigated, as shown in Figure 1c,d. Clearly, the intensity of the PA signal at the resonance frequency increases and then decreases with the length of the buffer cavity. The best length of the buffer cavity is 15 mm. However, as the radius of the buffer cavity increases from 7 to 12 mm, the intensity of the sound pressure just increases slightly. In order to obtain an open-ended condition at both ends of the resonant cavity, the buffer cavity needs a large length and radius to avoid the disturbance of solution flow in the acoustic field [31]. From the above FEM simulation results, the resonance frequency of the PA signals is from 3 to 6 kHz.

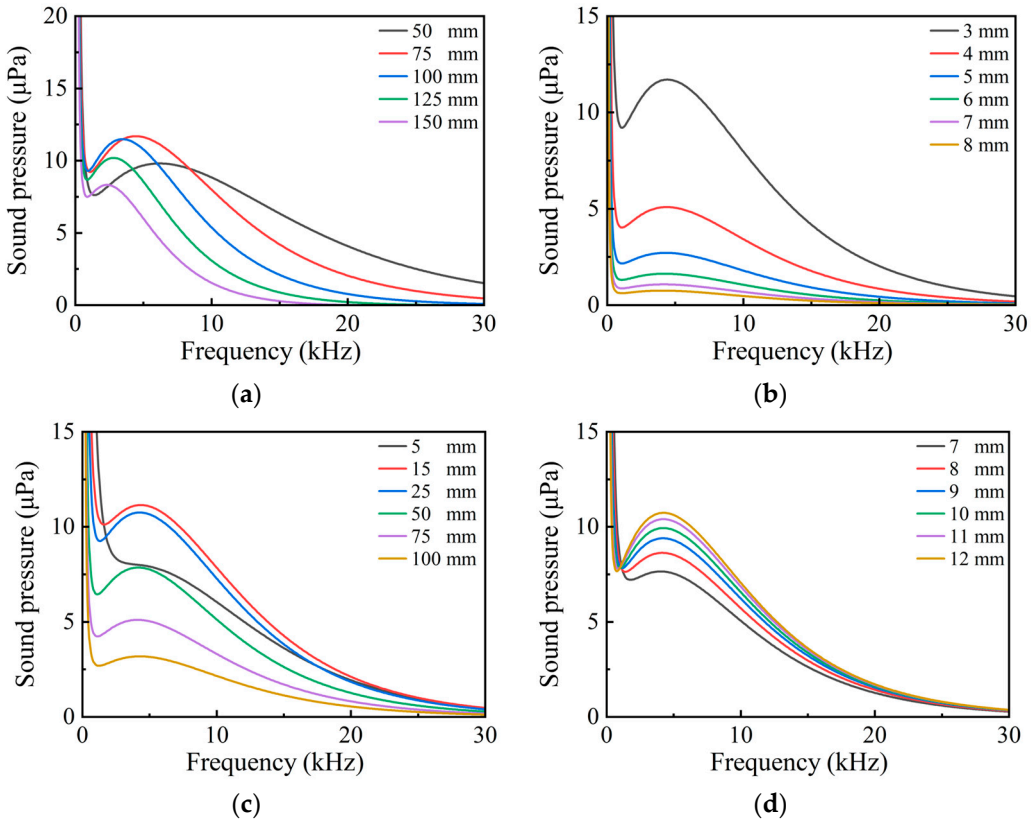

Figure 1. Simulated PA signal from different geometry sizes of the PA cell. (**a**) Resonant cavity lengths; (**b**) resonant cavity radii; (**c**) buffer cavity lengths; (**d**) buffer cavity radii.

For the PA cell, the noise is another important parameter that needs to be considered. The amount of noise resulting from the PA cell windows and the ambient noise from the buffer volume to the resonator cavity is called the "noise transmission coefficient" α_n, which can be determined as follows [32,33]:

$$\alpha_n = \frac{4}{4\cos^2(kL_b) + \left[\left(\frac{S_2}{S_1}\right) + \left(\frac{S_1}{S_2}\right)\right]^2 \sin^2(kL_b)} \tag{10}$$

where S_1 and S_2 are the cross-sectional area of the resonant cavity and the buffer cavity and k is the acoustic wave number. Figure 2 shows the noise transmission coefficient with different buffer cavity lengths and radii. The value of the noise transmission coefficient closer to 0 indicates the better noise reduction performance of the PA cell. Obviously, the noise transmission coefficient decreases as the buffer cavity's length and radius increases. In order to achieve a balance between the noise transmission coefficient and the volume of the PA cell, the length and radius of the buffer cavity are selected to be about 15 mm and 9 mm, respectively. Hence, we determined the size of the PA cell to be L_r = 75 mm, R_r = 3 mm, L_b = 15 mm, and R_b = 9 mm. Under this size of the PA cell, the intensity of the sound pressure at the resonance frequency is about 13.7 μPa.

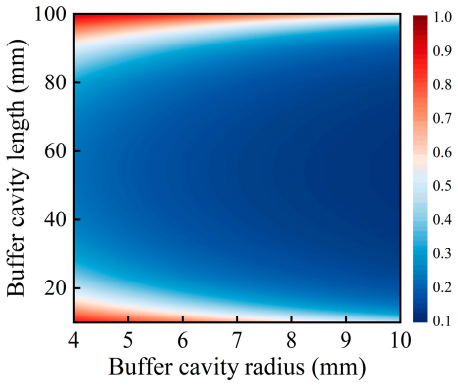

Figure 2. Noise transmission coefficient at different buffer cavity sizes.

3. C_2H_2 Concentration Measurement

The schematic diagram of the PA sensor system is shown in Figure 3. It was mainly composed of a light modulation unit, a PA signal acquisition unit, and a data processing unit. The function of the light modulation unit is to control the laser output power, the center wavelength, the bandwidth, and the pulse frequency. The PA signal acquisition unit consisted of a closed C_2H_2–Oil mixed solution PA cell and a Fabry–Perot cavity (F-P) microphone. The detection diaphragm of the F-P microphone just came into contacted with the upper edge of the C_2H_2–Oil mixed solution. The F-P microphone cannot be immersed into the solution because it could disturb the PA signal in the PA cell. The collected PA signal was transmitted to the data processing unit, stored, processed, and then displayed on a computer.

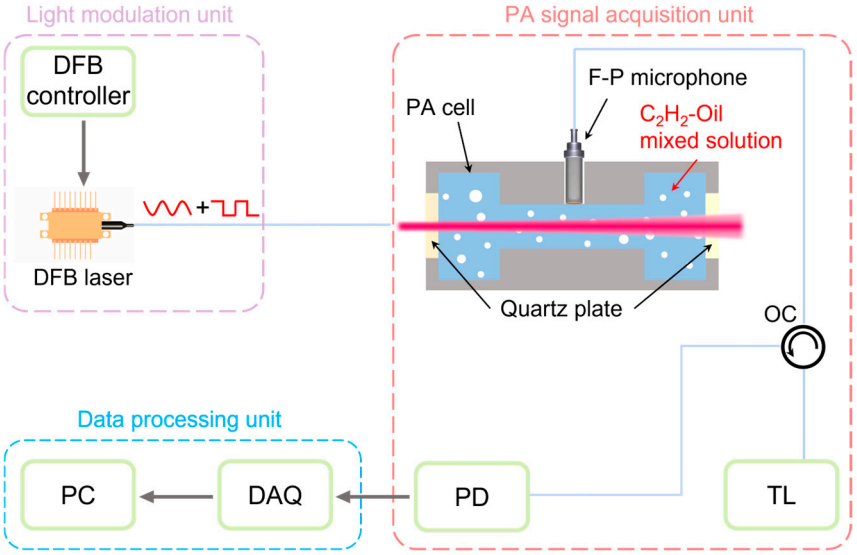

Figure 3. Experimental schematic illustration of the PA sensor system. (DFB: distributed feedback laser, OC: optical circulator, TL: tunable laser, PD: photoelectric detector, DAQ: data acquisition, and PC: personal computer).

The light modulation unit used a narrow line width 1529.18 nm tunable DFB laser and a controller. In Figure 4a, 1529.18 nm (6540.45 1/cm) is one of the strong absorption peaks of C_2H_2 in the near-infrared region (4000~13,333 1/cm). The absorption coefficient of C_2H_2 at 1529.18 nm is about 5.55×10^{-1} 1/cm. Although the absorption of C_2H_2 under 6580 cm^{-1} is slightly stronger than 6540 cm^{-1} (Figure 4a), the 1529 nm DFB laser was commonly used in gas sensing as it was easy to buy. It should be noticed that the absorption coefficient of the C_2H_2–Oil mixed solution had significant differences compared to that in

a gaseous environment [34], and the change in the absorption coefficient only influenced the intensity of the PA signal. In this work, the measurement of the C_2H_2 concentration was conducted based on the calibration curve of the PA signal under different C_2H_2 concentrations, which is nearly independent of the absolute value of the intensity of the PA signal. The built-in function generator of the DFB laser could superimpose a square wave signal within the driving current. Hence, the DFB laser could output a continually modulated light pulse signal into the PA cell. The intensity of the PA signal as a function of the modulation bandwidth is shown in Figure 4b. The result indicates that the wider modulation bandwidth is better. Hence, in our experiment, the modulation bandwidth of the DFB laser was selected at about 62 GHz. The modulated light pulse signal was inserted into the PA cell through a collimator. Based on the FEM simulation result in Figure 1, the geometry size of the PA cell was L_r = 75 mm, R_r = 3 mm, L_b = 15 mm, and R_b = 9 mm. The collection of the PA signal was accomplished by the F-P microphone, which was operated with a tunable 1550 nm DFB laser and a photodetector (PD). The schematic diagram of the F-P microphone is shown in Figure 4c. The F-P cavity was constructed between the 100 nm thickness gold diaphragm and the end of the optical fiber. The working principle of the proposed F-P microphone is the F-P interference. The PA signal is loaded onto the surface of the gold diaphragm, which could have a deformation under the mechanical load from the PA signal. Hence, the intensity variation in the PA signal was turn into the length change in the F-P cavity and then induced the change in the interference signal. Figure 4d shows the sensitivity tests results of the F-P microphone in the sound signal frequency range from 1.0 to 7.0 kHz. Compared with the conventional condenser and piezo-ceramic microphones, the sensitivity of the F-P microphone (~−5 dB) improved by about one order of magnitude [35].

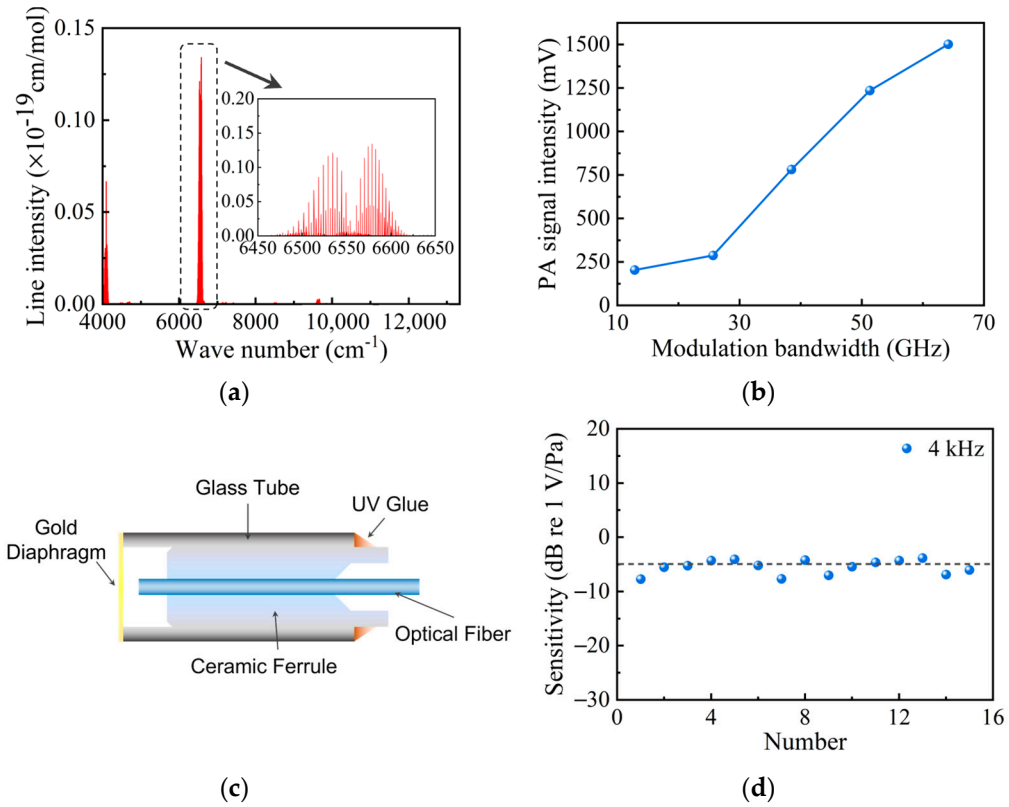

Figure 4. Performances of the DFB laser and the F-P microphone. (**a**) Absorption spectrum of C_2H_2 in the near-infrared region; (**b**) intensity of the PA signal as a function of the light modulation frequency. (**c**) Schematic diagram of the F-P microphone; (**d**) sensitivity of the F-P microphone.

Before the measurement, the concentration of C_2H_2 in the C_2H_2–Oil mixed solution samples was calibrated using the gas chromatograph. The model of the dielectric oil is KI 25X transformer oil. The C_2H_2 concentration range was from 0 to 100 mL/L. During the measurement, the temperature of the C_2H_2–Oil mixed solution was kept at about 300 K, and the pressure in the PA cell was kept at standard atmospheric pressure. Each measurement required cleaning the PA cell and then letting in the C_2H_2–Oil mixed solution sample for 10 min through an oil pump. The intensity of the PA signal from the different concentrations of C_2H_2 is shown in Figure 5a. Obviously, the peak intensity of the PA signal appeared near the resonance frequency of the PA cell at about 4 kHz, which is consistent with our FEM simulation results in Figure 1. The resonance frequency of the PA signal was dominated by the length of the PA cell. Although the length of the PA cell was unchanged in our experiments, the environmental temperature and vibration may be affected by the modulation frequency of the incident light and sound wave transport in the C_2H_2–Oil mixed solution. As a result, the frequency corresponding to the PA signal peak showed a slight change. The inverse relationship is seen for the light modulation frequency below 3 kHz in Figure 5a. This result reflects the sensor system working in the non-resonant mode because of the decrease in photoenergy with increasing light modulation frequency. When the light modulation frequency is higher than 3.5 kHz, the contribution of the resonant effect in the PA cell makes the relationship between the intensity of the PA signal and the resonance frequency of the PA cell exhibits a Lorentzian line shape. Figure 5b shows the calibration curve of different C_2H_2 concentrations versus the intensity of the PA signal. The intensity of the PA signal (p) in the PA cell can be represented as follows [36]:

$$p = I_m \alpha C_{cell} \tag{11}$$

where C_{cell} is the PA cell constant. The light absorption coefficient α rises linearly with the C_2H_2 concentration. Hence, the intensity of the PA signal should have a linear relationship with the C_2H_2 concentration. Clearly, in Figure 5b, the intensity of the PA signal from the C_2H_2–Oil mixed solution rises almost linearly with the concentration of C_2H_2 from 25 to 100 mL/L. From the slope of the calibration curve, the resolution of the PA sensor system is about 9.62 mV/mL·L^{-1}. However, within the low C_2H_2 concentration range (0 to 25 mL/L), the linear relationship between the intensity of the PA signal and the concentration of C_2H_2 is not ideal. The reason may be that when the concentration of C_2H_2 is lower than 25 mL/L, the sensitivity of the F-P microphone is not good. The noise equivalent pressure (NEP) of the microphone can be calculated as follows:

$$\mathrm{NEP} = \frac{N}{S} \tag{12}$$

where N and S represent the noise spectrum (Figure 5c) and the sound pressure sensitivity of the microphone, respectively. The lower value of the NEP indicates higher detection sensitivity. The values of the NEP from the F-P microphone are shown in Figure 5d. Obviously, the detection sensitivity of the F-P microphone decreases with decreasing C_2H_2 concentration.

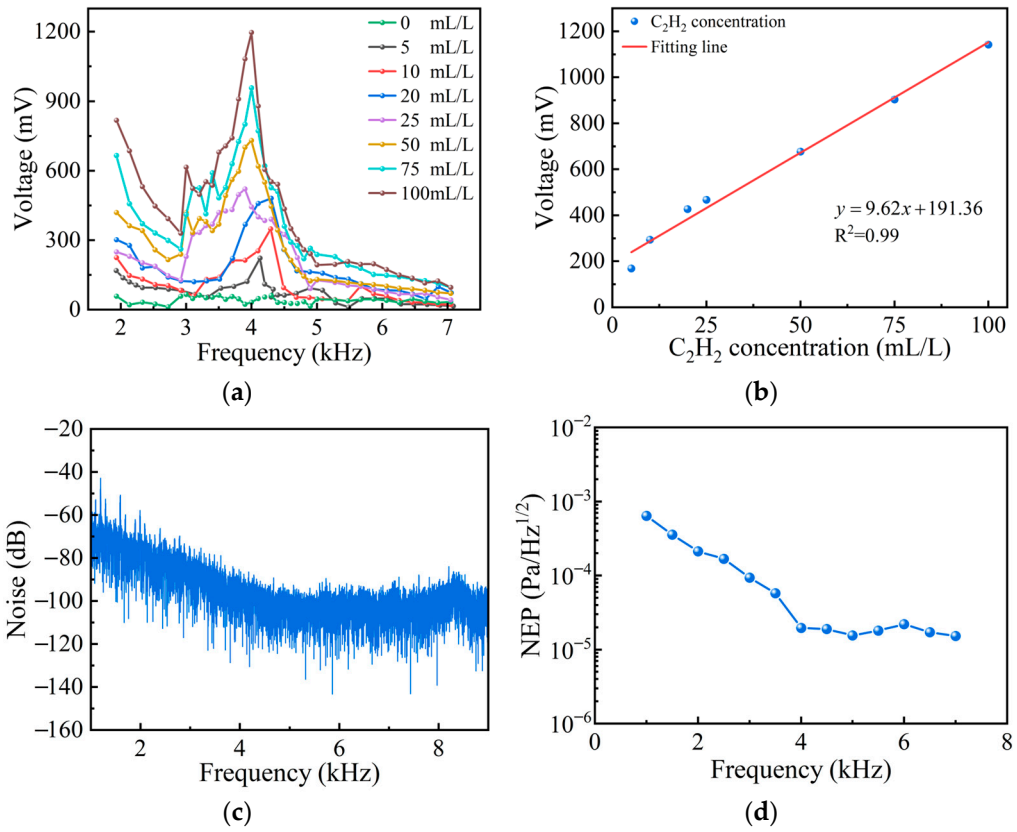

Figure 5. Performances of the PA sensor system. (**a**) PA signal from different concentrations of C_2H_2; (**b**) calibration curve of the intensity of the PA signal; (**c**) background noise of the PA sensor system; (**d**) NEP testing results of the microphone.

Figure 6 shows the overlayers of the frequency response curve from the FEM simulation and the experiments. The C_2H_2 concentration is about 100 mL/L. Clearly, the peak width of the frequency response curve from the FEM simulation is wider than that of the experiments. In the FEM simulation, the peak width is dominated by the isothermal compression coefficient, which represents the relative change rate of the thermal balance density for the dielectric oil medium under the pressure. Hence, the value of the thermal equilibrium density is a variable because its dependents on the temperature of the dielectric oil during the FEM simulation. This process represents the heat exchange between the adjacent medium regions through thermal conduction and induces a thermal relaxation process. As a result, the simulated peak width of the frequency response curve is wider than that of the experiments. It should be noticed that the value of the resonance frequency from the FEM simulation is a good match with the experiments. In fact, the result of the resonance frequency from the FEM simulation is more important.

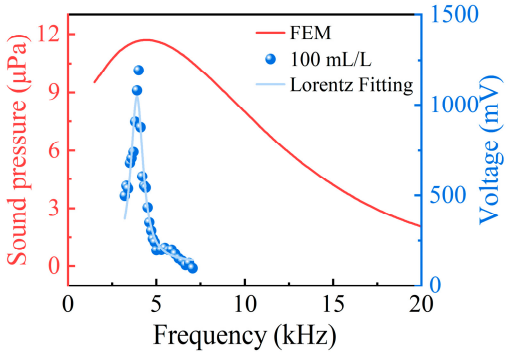

Figure 6. Frequency response curve from the FEM simulation and experiments.

4. Error Analysis and Stability Tests

There are two possible reasons for the potential sources of measurement error from the PA sensor system: (1) The intensity of the PA signal is sensitive to the output wavelength and power of the DFB laser. Figure 7a shows the stability tests of the DFB laser. Although a laser controller was used to keep the working temperature and drive the current of the DFB laser, the output of the DFB laser still fluctuated slightly with time. As a results, the intensity of the PA signal also fluctuated and then induced the error in the measurement. (2) The sensitivity of the F-P microphone is influenced by the environment temperature and mechanical vibration (Figure 7b). Although the PA sensor system was placed in the soundproof box, the performances of the F-P microphone were also affected by the slight change in the working environment, which induced the error in the measurement.

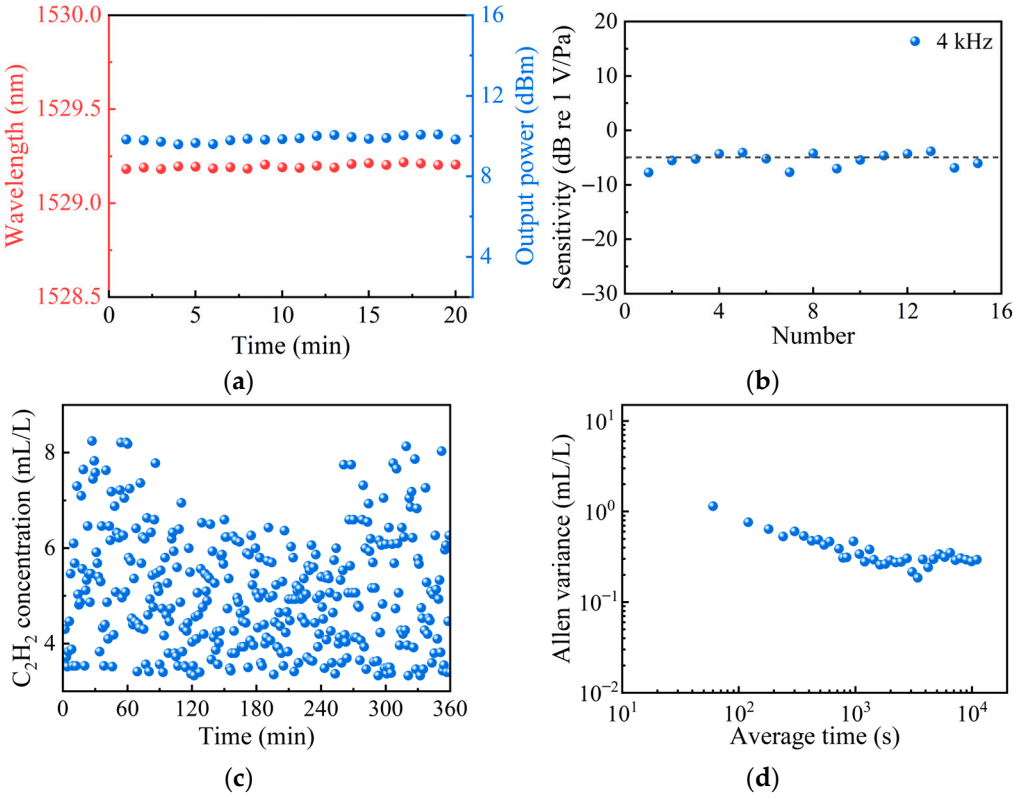

Figure 7. Stability tests of the PA sensor system. (**a**) Output power and center wavelength stability of the DFB laser; (**b**) sensitivity and stability of the F-P microphone; (**c**) Continuous measurement with the 5 mL/L C_2H_2–Oil mixed solution; (**d**) Allan variance calculation results.

To evaluate the repeatability and measurement limit of the PA sensor system, multiple measurements were carried out (Figure 7c). A continuous measurement of the intensity of the PA signal using the 5 mL/L C_2H_2–Oil mixed solution sample at time intervals of 1 min was performed 360 times. The Allan variance results from the continuous tests are shown in Figure 7d. Clearly, the measurement limit of the PA sensor system could achieve about 0.2 mL/L when the averaging time is about 3400 s.

5. Discussion and Conclusions

Commonly used technologies for measuring the C_2H_2 concentration include non-spectroscopic and spectroscopic methods. Among the non-spectroscopic methods, gas chromatography (GC) and chemical sensors are widely used. The GC is now widely used in measuring the dissolved C_2H_2 concentration. The GC is highly sensitive, but it requires a long measuring time and calibration before measurement. Chemical sensors

have several distinct advantages such as high sensitivity and good selectivity. However, it also has some inherent drawbacks such as poor repeatability and sensitivity for a working environment [37]. The spectroscopic methods include Fourier infrared spectroscopy (FTIR), Raman spectroscopy (RS), and tunable diode laser absorption spectroscopy (TDLAS) [38]. These spectroscopic methods have some advantages such as high sensitivity and a rapid detection time without the need for calibration. However, it still has some challenges such as susceptible to environmental damage and electromagnetic interference. Importantly, the above technologies are all reliant on the gas–liquid separation process, which could induce a long detection time and complicate the overall system setup. The comparison of our proposed PA method with the GC, RS, FTIR, and TDLAS methods is shown in Table 2. Obviously, the proposed PA method has the distinct advantages of a short measurement time and low system complexity without degassing. Although the measurement limit (200 μL/L) is higher than the standard for the oil-filled electrical equipment (1 μL/L), it could be improved in future studies.

Table 2. Comparison of the dissolved gas measurement methods.

Performance Index	GC [39]	RS [40]	FTIR [41]	TDLAS [42]	Our PAS
Limit of Detection (C_2H_2)	0.05 μL/L	5 μL/L	0.1 μL/L	0.5 μL/L	0.2 mL/L
Measurement Time	30 min	30 min	30 min	30 min	20 s
System Complexity	High	High	Moderate	Moderate	Low
Degassing Required	Yes	Yes	Yes	Yes	No

It should be noticed that the method reported here could also measure the other trace gas concentrations. In the measurement, the center wavelength of the incident light must match the absorption peak of the gas. For future studies, the performance of the PA sensor system could be improved by increasing the incident light power, decreasing the radius of the PA cell, redesigning the microphone, and optimizing the signal processing process.

In this paper, we studied the PA signal in different concentrations of the C_2H_2–Oil mixed solution. It has been demonstrated that the intensity of the PA signal is proportional to the concentration of C_2H_2 from 0 to 100 mL/L. The Allan variance results from the continuous tests indicate that the measurement limit of the PA sensor system is about 0.2 mL/L. Compared with conventional PA sensors, the proposed PA sensor could shorten the measurement time and decrease the volume of equipment due to the removal of the degassing component.

Author Contributions: Z.R., Z.M. and S.D. designed the experiments. Z.R. and J.K. contributed to sample preparation. Z.R., Z.M., J.K. and S.D. performed the experiments. Z.R., H.L., X.W. and M.L. contributed to data analysis. Z.R., L.L., S.D. and M.L. wrote the paper. All authors have read and agreed to the published version of the manuscript.

Funding: National Natural Science Foundation of China (62304161); Key R&D Program of Hubei Province (2024BAB009).

Data Availability Statement: Data underlying the results presented in this paper are not publicly available at this time but may be obtained from the authors upon reasonable request.

Conflicts of Interest: Authors Jian Ke, Zhiwen Ming, and Shuo Deng were employed by the company Wuhan Yusheng Optoelectronic Co., Ltd. The remaining authors declare that the research was conducted in the absence of any commercial or financial relationships that could be construed as a potential conflict of interest.

References

1. Chen, T.; Ma, F.; Zhao, Y.; Zhao, Y.; Wan, L.; Li, K.; Zhang, G. Portable ppb-level acetylene photoacoustic sensor for transformer on-field measurement. *Optik* **2021**, *243*, 167440. [CrossRef]
2. Li, C.; Qi, H.; Zhao, X.; Guo, M.; An, R.; Chen, K. Multi-pass absorption enhanced photoacoustic spectrometer based on combined light sources for dissolved gas analysis in oil. *Opt. Lasers Eng.* **2022**, *159*, 107221. [CrossRef]
3. Mao, Z.; Wen, J. Detection of dissolved gas in oil–insulated electrical apparatus by photoacoustic spectroscopy. *IEEE Electr. Insul. Mag.* **2015**, *31*, 7–14. [CrossRef]
4. Zhu, Q.; Yin, Y.; Wang, Q.; Wang, Z.; Li, Z. Study on the online dissolved gas analysis monitor based on the photoacoustic spectroscopy. In Proceedings of the 2012 IEEE International Conference on Condition Monitoring and Diagnosis, Bali, Indonesia, 23–27 September 2012; IEEE: Piscataway, NJ, USA, 2012; pp. 433–436.
5. Bustamante, S.; Manana, M.; Arroyo, A.; Castro, P.; Laso, A.; Martinez, R. Dissolved gas analysis equipment for online monitoring of transformer oil: A review. *Sensors* **2019**, *19*, 4057. [CrossRef] [PubMed]
6. Palzer, S. Photoacoustic-based gas sensing: A review. *Sensors* **2020**, *20*, 2745. [CrossRef]
7. Boschetti, A.; Bassi, D.; Iacob, E.; Iannotta, S.; Ricci, L.; Scotoni, M. Resonant photoacoustic simultaneous detection of methane and ethylene by means. of a 1.63-μm diode laser. *Appl. Phys. B* **2002**, *74*, 273–278. [CrossRef]
8. Wolff, M.; Harde, H. Photoacoustic spectrometer based on a DFB-diode laser. *Infrared Phys. Technol.* **2000**, *41*, 283–286. [CrossRef]
9. Besson, J.P.; Schilt, S.; Thévenaz, L. Sub-ppm multi-gas photoacoustic sensor. *Spectrochim. Acta Part A Mol. Biomol. Spectrosc.* **2006**, *63*, 899–904. [CrossRef]
10. Goto, M.; Iguchi, Y.; Ono, K.; Ando, A.; Takeshi, F.; Matsunaga, S.; Yasuno, Y.; Tanioka, K.; Tajima, T. High-performance condenser microphone with single-crystalline silicon diaphragm and backplate. *IEEE Sens. J.* **2006**, *7*, 4–10. [CrossRef]
11. Lindley, R.E.; Parkes, A.M.; Keen, K.A.; McNaghten, E.D.; Orr-Ewing, A.J. A sensitivity comparison of three photoacoustic cells containing a single microphone, a differential dual microphone or a cantilever pressure sensor. *Appl. Phys. B* **2007**, *86*, 707–713. [CrossRef]
12. Chen, K.; Yu, Q.; Gong, Z.; Guo, M.; Qu, C. Ultra-high sensitive fiber-optic Fabry-Perot cantilever enhanced resonant photoacoustic spectroscopy. *Sens. Actuators B Chem.* **2018**, *268*, 205–209. [CrossRef]
13. Zhang, C.; Qiao, S.; Ma, Y. Highly sensitive photoacoustic acetylene detection based on differential photoacoustic cell with retro-reflection-cavity. *Photoacoustics* **2023**, *30*, 100467. [CrossRef] [PubMed]
14. Yun, Y.; Chen, W.; Wang, Y.; Pan, C. Photoacoustic detection of dissolved gases in transformer oil. *Eur. Trans. Electr. Power* **2008**, *18*, 562–576. [CrossRef]
15. Kitamori, T.; Sawada, T. Theoretical Analysis of Frequency Characteristics of Photoacoustic Signal in Liquids. *Jpn. J. Appl. Phys.* **1982**, *21*, L285. [CrossRef]
16. Nosaka, Y.; Tokunaga, E. Development of photoacoustic spectroscopy with a piezofilm. *Appl. Opt.* **2007**, *46*, 4289–4293. [CrossRef] [PubMed]
17. Zheng, H.; Li, Y.; Chen, Y.; Wang, Z.; Dai, J. Experimental Research on Measuring the Concentration of CO_2 in Gas-Liquid Solution Based on PZT Piezoelectric-Photoacoustic Spectroscopy. *Sensors* **2022**, *22*, 936. [CrossRef]
18. Wang, Y.; Ma, G.; Xie, Y.; Chen, Z.; Zheng, D.; Qin, W. Direct Detection of Oil-dissolved Acetylene Without Oil-gas Separation. *Proc. CSEE* **2023**, *43*, 8151–8160.
19. Bakar, N.A.; Abu-Siada, A.; Islam, S. A review of dissolved gas analysis measurement and interpretation techniques. *IEEE Electr. Insul. Mag.* **2014**, *30*, 39–49. [CrossRef]
20. Li, Z.; Liu, J.; Ning, Z.; Xu, H.; Miao, J.; Pan, Y.; Yang, C.; Fang, Y. Compact gas cell for simultaneous detection of atmospheric aerosol optical properties based on photoacoustic spectroscopy and integrating sphere scattering enhancement. *Photoacoustics* **2024**, *36*, 100591. [CrossRef]
21. Duggen, L.; Lopes, N.; Willatzen, M.; Rubahn, H.G. Finite element simulation of photoacoustic pressure in a resonant photoacoustic cell using lossy boundary conditions. *Int. J. Thermophys.* **2011**, *32*, 774–785. [CrossRef]
22. Shtemler, Y.M.; Shreiber, I.R. Heat transfer in sound propagation and attenuation through gas–liquid polyhedral foams. *Int. Commun. Heat Mass Transf.* **2006**, *33*, 571–579. [CrossRef]
23. He, Q.; Wang, Q.; Lv, P.; Lu, Z.; Lv, N.; Zhao, H.; Tao, W. Liquid photoacoustic sensing with high sensitivity by temperature compensated differential detection method. *Appl. Phys. Express* **2020**, *13*, 117001. [CrossRef]
24. Xiong, S.; Yin, X.; Wang, Q.; Xia, J.; Chen, Z.; Lei, H.; Yan, X.; Zhu, A.; Qiu, F.; Chen, B.; et al. Photoacoustic Spectroscopy Gas Detection Technology Research Progress. *Appl. Spectrosc.* **2024**, *78*, 139–158. [CrossRef]
25. Mannoor, M.; Hwang, J.; Kang, S. Numerical study of geometrical effects on the performance of an H-type cylindrical resonant photoacoustic cell. *J. Mech. Sci. Technol.* **2018**, *32*, 5671–5683. [CrossRef]
26. Kitamori, T.; Fujii, M.; Sawada, T.; Gohshi, Y. Frequency characteristics of photoacoustic signals generated in liquids. *J. Appl. Phys.* **1984**, *55*, 4005–4009. [CrossRef]

27. Cai, Y.; Arsad, N.; Li, M.; Wang, Y. Buffer structure optimization of the photoacoustic cell for trace gas detection. *Optoelectron. Lett.* **2013**, *9*, 233–237. [CrossRef]
28. Dombek, G.; Nadolny, Z. Influence of paper type and liquid insulation on heat transfer in transformers. *IEEE Trans. Dielectr. Electr. Insul.* **2018**, *25*, 1863–1870. [CrossRef]
29. Mia, S.; Ohno, N. Prediction of pressure–viscosity coefficient of lubricating oils based on sound velocity. *Lubr. Sci.* **2009**, *21*, 343–354. [CrossRef]
30. Rothman, L.S.; Gordon, I.E.; Babikov, Y.; Barbe, A.; Benner, D.C.; Bernath, P.F.; Birk, M.; Bizzocchi, L.; Boudon, V.; Brown, L.R.; et al. The HITRAN2012 molecular spectroscopic database. *J. Quant. Spectrosc. Radiat. Transf.* **2013**, *130*, 4–50. [CrossRef]
31. Cheng, G.; Cao, Y.; Tian, X.; Cao, Y.; Liu, K. Influence of photoacoustic cell geometrical shape on the performance of photoacoustic spectroscopy. *Spectrosc. Spectr. Anal.* **2020**, *40*, 2345–2351.
32. Kinsler, L.E.; Frey, A.R.; Coppens, A.B.; Sanders, J.V. *Fundamentals of Acoustics*; John Wiley & Sons: Hoboken, NJ, USA, 2000.
33. Tavakoli, M.; Tavakoli, A.; Taheri, M.; Saghafifar, H. Design, simulation and structural optimization of a longitudinal acoustic resonator for trace gas detection using laser photoacoustic spectroscopy (LPAS). *Opt. Laser Technol.* **2010**, *42*, 828–838. [CrossRef]
34. Jiang, J.; Wang, Z.; Ma, G.; Song, H.; Zhang, C. Direct detection of acetylene dissolved in transformer oil using spectral absorption. *Optik* **2019**, *176*, 214–220. [CrossRef]
35. Wu, G.; Xiong, L.; Dong, Z.; Liu, X.; Cai, C.; Qi, Z.M. Development of highly sensitive fiber-optic acoustic sensor and its preliminary application for sound source localization. *J. Appl. Phys.* **2021**, *129*, 164504. [CrossRef]
36. Dumitras, D.C.; Dutu, D.C.; Matei, C.; Magureanu, A.M.; Petrus, M.; Popa, C. Laser photoacoustic spectroscopy: Principles, instrumentation, and characterization. *J. Optoelectron. Adv. Mater.* **2007**, *9*, 3655.
37. Guan, W.; Tang, N.; He, K.; Hu, X.; Li, M.; Li, K. Gas-sensing performances of metal oxide nanostructures for detecting dissolved gases: A mini review. *Front. Chem.* **2020**, *8*, 76. [CrossRef] [PubMed]
38. Dai, J.; Luo, B.; Shen, X.; Han, W.; Cui, R.; Wu, J.; Zhang, H.; Xiao, W.; Zhong, Z.; Dong, L.; et al. A review of optical gas sensing technology for dissolved gas analysis in transformer oil. *Front. Phys.* **2025**, *13*, 1547563. [CrossRef]
39. Fan, J.; Wang, F.; Sun, Q.; Bin, F.; Ding, J.; Ye, H. SOFC detector for portable gas chromatography: High-sensitivity detection of dissolved gases in transformer oil. *IEEE Trans. Dielectr. Electr. Insul.* **2017**, *24*, 2854–2863. [CrossRef]
40. Chen, W.; Zhao, L.; Peng, S.; Lu, J.; Zhou, J. Analysis of Dissolved Gas in Transformer Oil Based on Laser Raman Spectroscopy. *Proc. CSEE* **2014**, *34*, 2485–2492.
41. Tang, X.; Wang, W.; Zhang, X.; Wang, E.; Li, X. On-line analysis of oil-dissolved gas in power transformers using Fourier transform infrared spectrometry. *Energies* **2018**, *11*, 3192. [CrossRef]
42. Chen, Y.; Wang, Z.; Li, Z.; Zheng, H.; Dai, J. Development of an online detection setup for dissolved gas in transformer insulating oil. *Appl. Sci.* **2021**, *11*, 12149. [CrossRef]